




## Rebuilding the vibrational wavepacket in TRAS using attosecond X-ray pulses

Chao Wang<sup>1</sup>, Maomao Gong<sup>1</sup>, Xi Zhao<sup>1</sup>, Quan Wei Nan<sup>1</sup>, Xin Yue Yu<sup>1</sup>, Yongjun Cheng<sup>1</sup>, Victor Kimberg <sup>2</sup>, Xiao-Jing Liu<sup>3</sup>, Oriol Vendrell <sup>4</sup>, Kiyoshi Ueda<sup>3,5</sup> & Song Bin Zhang <sup>1</sup>✉

Time-resolved X-ray photoelectron spectroscopy (TXPS) is a well-established technique to probe coherent nuclear wavepacket dynamics using both table-top and free-electron-based ultrafast X-ray lasers. Energy resolution, however, becomes compromised for a very short pulse duration in the sub-femtosecond range. By resonantly tuning the X-ray pulse to core-excited states undergoing Auger decay, this drawback of TXPS can be mitigated. While resonant Auger-electron spectroscopy (RAS) can recover the vibrational structures not hidden by broadband excitation, the full reconstruction of the wavepacket is a standing challenge. Here, we theoretically demonstrate how the complete information of a nuclear wavepacket, i.e., the populations and relative phases of the vibrational states constituting the wavepacket, can be retrieved from time-resolved RAS (TRAS) measurements. Thus, TRAS offers key insights into coupled nuclear and electronic dynamics in complex systems on ultrashort timescales, providing an alternative to leverage femtosecond and attosecond X-ray probe pulses.

<sup>1</sup>School of Physics and Information Technology, Shaanxi Normal University, Xi'an 710119, China. <sup>2</sup>Theoretical Chemistry and Biology, Royal Institute of Technology, Stockholm 10691, Sweden. <sup>3</sup>School Physical Science and Technology, ShanghaiTech University, Shanghai 201210, China. <sup>4</sup>Theoretical Chemistry, Institute of Physical Chemistry, Heidelberg University, 69120 Heidelberg, Germany. <sup>5</sup>Department of Chemistry, Tohoku University, Sendai 980-8578, Japan. ✉email: [song-bin.zhang@snnu.edu.cn](mailto:song-bin.zhang@snnu.edu.cn)

Time-resolved pump-probe experiments provide a powerful tool for tracking ultrafast electronic and nuclear dynamics, where the evolution of the nuclear (vibrational) wavepacket, which may go through the conical intersection in the excited states populated by the pump pulse, can be precisely unveiled aided by the advanced theoretical simulations<sup>1–7</sup>. Notable techniques such as time-resolved photoelectron spectroscopy<sup>1</sup> and high-harmonic interferometry<sup>2</sup> allow to discern and track coupled vibrational and electronic dynamics, and attosecond transient absorption spectroscopy<sup>3</sup> has enabled direct mapping of non-adiabatic curve-crossing dynamics. These techniques have been successfully implemented in numerous laboratories using ultrafast lasers.

The recent development of X-ray free-electron laser sources (XFELs) has introduced new possibilities for pump-probe techniques<sup>8–14</sup>, resulting in time-resolved X-ray absorption spectroscopy<sup>15,16</sup>, time-resolved X-ray photoelectron spectroscopy (TXPS)<sup>17–21</sup>, time-resolved X-ray photoelectron diffraction<sup>22–24</sup>, ultrafast X-ray Raman spectroscopy<sup>25,26</sup>, ultrafast X-ray scattering<sup>27–32</sup>, femtosecond X-ray solution scattering<sup>33–35</sup> etc., which have been extensively utilized at XFEL facilities to investigate ultrafast electronic and nuclear dynamics<sup>36</sup>.

As the temporal duration of X-ray pulses decreases from tens of femtoseconds to hundreds and tens of attoseconds, however, the vibrational structures in TXPS become unresolved due to the broad bandwidth of attosecond X-ray pulses<sup>17,37,38</sup>.

If the incoming X-ray photon is tuned to resonantly promote a core electron to an unoccupied orbital to trigger the resonant Auger decay, the Auger lifetime broadening dominates the resolution of the resonant Auger-electron spectroscopy (RAS), and thus vibrational structures involved in RAS do survive<sup>39–41</sup>. This has been demonstrated as well for transient X-ray absorption of optically phototriggered molecules using a core-to-valence excitation<sup>42</sup>. Therefore, time-resolved RAS (TRAS) as a probe technique can become an invaluable complementary technique to TXPS<sup>43,44</sup>, e.g., to follow vibrational and vibronic dynamics with femtosecond to attosecond time resolution.

Attosecond transient absorption spectroscopy (ATAS) has been successfully used to reconstruct the coherent valence electron motion between states  $\text{Kr}^+(4p_{1/2}^-)$  and  $\text{Kr}^+(4p_{3/2}^-)$ <sup>45</sup> and within doubly excited states in He<sup>46</sup>. More recently, this technique has been used to reconstruct the  $c_1|J_1\rangle + c_2|J_2\rangle$  rotational wavepacket of  $\text{H}_2$  and  $\text{D}_2$  molecules<sup>47</sup>; ATAS also shows great potential in disentangling complex multi-mode nuclear dynamics for polyatomic molecules<sup>48,49</sup>. The delay-dependent kinetic energy release technique is able, as well, to resolve the phase interference of a prepared ionic vibrational wavepacket of  $\text{H}_2^+$ <sup>50</sup>, whereas another recently proposed approach uses time-resolved photoelectron spectroscopy from molecular autoionization<sup>51</sup> to reconstruct the time-dependent electronic wavepacket, also of  $\text{H}_2^+$ . High-harmonic generation spectroscopy has also been used to reconstruct the electronic wave packet that describes charge migration in the HCCI molecule<sup>52</sup>.

As described above, the reconstruction of femto- to attosecond vibronic and electronic wavepacket dynamics is one of the central goals of femtochemistry and attosecond science<sup>45–52</sup>, and given the broad interest of tracking vibronic at conical intersections in ultrafast photochemistry<sup>17,49</sup>, this research may pave the way for broad application of femtosecond and attosecond X-ray probe pulses. Here, we theoretically explore the application of attosecond X-ray pulses and demonstrate that the detailed dynamics of a coherent vibrational wavepacket can be fully reconstructed from TRAS using attosecond X-ray pulses. Namely, the oscillatory nuclear wavepacket motion of a showcased diatomic molecule is reconstructed by TRAS by fitting a simple time-dependent

formula, and the relative populations and phases of the involved vibrational states are extracted with high accuracy.

## Results and Discussion

**TRAS using attosecond X-ray pulses.** We consider a CO molecule as illustrated in Fig. 1a. A nuclear wavepacket of state  $5\sigma^{-1}\pi^*A^1\Pi$  is generated by exciting CO from its ground state  $X^1\Sigma^+$  using a 8.0 fs UV pulse with central frequency of 8.0 eV and Rabi-frequency of 0.002 a.u. This wavepacket is probed by a time-delayed ( $\Delta t$ ) resonant attosecond X-ray pulse ( $\tau = 1$  fs and  $\omega = 280.0$  eV) initiating resonant Auger decay from the core-excited state  $C1s^{-1}\pi^*1\Pi$ . We then calculate the TRAS signal, which depends on the pump-probe delay  $\Delta t$  and corresponds to the Auger decay to the  $1\pi^{-1}2\Pi$  ionic state. In the calculations of TRAS, we employed the potential energy curves and the Auger width  $\Gamma = 0.08$  eV in reference<sup>53</sup>. The whole time evolution (about 100 fs) is much shorter than the rotational period of the CO molecule (about 8.64 ps) and thus the molecular rotation can be neglected during the interaction with the pulses and the Auger lifetime. The quantum time-dependent wave-packet method, accounting for the broad vibrational excitation by ultrashort pulses and lifetime-vibronic interference as implemented in references<sup>38,39,41,43,44,54,55</sup>, is used to calculate the RAS spectra, and the time-dependent Schrödinger equation is solved using the Heidelberg MCTDH package<sup>56</sup>.

Figure 1(c) shows the calculated TRAS spectra  $\sigma(\epsilon, \Delta t)$  (which has been given in the Supplementary Data). The joint coherent contributions between initial wavepacket and broad excited intermediate vibrational levels result in the diverse peak structures in the spectra<sup>44</sup>. The TRAS varies as a function of the pump-probe delay  $\Delta t$ , illustrating how TRAS is sensitive to the coherent nuclear wavepacket motion. The pattern of TRAS exhibits distinct ‘revival’ patterns with respect to  $\Delta t$  (The time zero  $\Delta t = 0$  is 24 fs from the pump pulse center). To further characterize the vibrational behavior, the time-dependent expectation value of inter-nuclear distance  $\langle R_{\text{CO}} \rangle(\Delta t)$  on state  $5\sigma^{-1}\pi^*A^1\Pi$  is shown in Fig. 1b.  $\langle R_{\text{CO}} \rangle(\Delta t)$  presents a pronounced ‘revival’ period of about 22 fs, corresponding to elongating and contracting dynamics of the nuclear wavepacket on state  $5\sigma^{-1}\pi^*A^1\Pi$ . Moreover, there is a slight decrease in amplitude with increasing  $\Delta t$ , suggesting the involvement of more than two vibrational states in the initial wavepacket. To investigate the sensitivity of TRAS to the vibronic dynamics, the Auger electron spectra are selected for cases where  $\langle R_{\text{CO}} \rangle(\Delta t)$  corresponds to left ( $L_1$  and  $L_2$ ) and right ( $R_1$  and  $R_2$ ) turning points, as shown in Fig. 1d. Minor differences are observed between the spectra obtained from the two turning points, further highlighting the sensitivity of TRAS to probe the nuclear wavepacket dynamics. Figure 1e depicts the time evolution of the Auger signals for selected Auger energies  $\epsilon = 270.9$  and  $271.1$  eV. Significantly, distinct beating evolution with varying structure is clearly observed, providing evidence consistent with the involvement of several vibrational states in the initial wavepacket.

**Rebuilding the initial wavepacket from TRAS.** Following the descriptions in section of Methods, if the molecule was initially in a coherent vibrational wavepacket in electronic state I, the amplitude of each vibrational state could be expressed as  $a_i^I(t) = c_i^I e^{i(\varphi_i^I - E_i^I t)}$ , where  $c_i^I$  and  $\varphi_i^I$  represent the initial coefficient (a positive number) and phase of the vibrational state  $|i^I\rangle$ , respectively. The amplitude of final state  $|f^F(q)\rangle$  is given by  $a_f^F(\epsilon, t) = \sum_i a_i^I(\Delta t) a_f^{F(i)}(\epsilon, t)$ . We can reach the following formula for the total Auger electron spectra from the coherent wavepacket

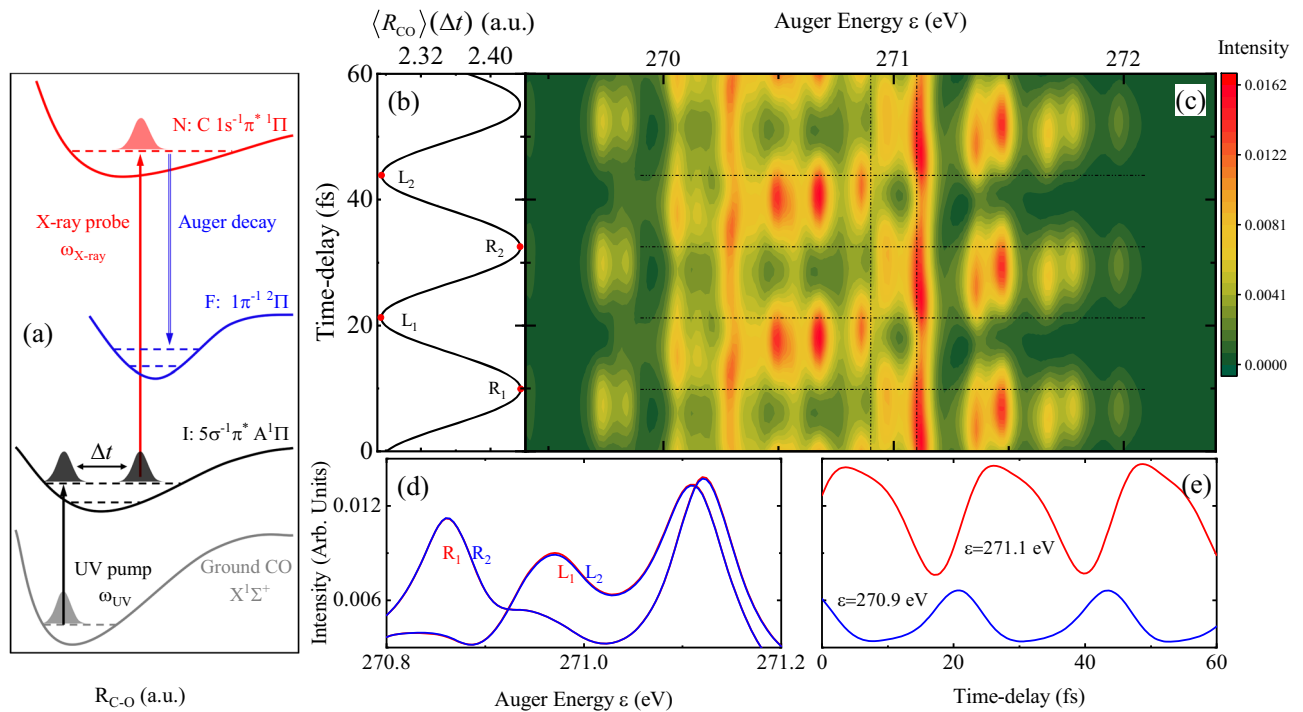


**Fig. 1 Time-resolved resonant Auger-electron spectroscopy of CO.** **a** Illustration of TRAS by UV-pump and X-ray probe to trigger the resonant Auger decay, detecting the nuclear wavepacket of state I ( $5\sigma^{-1}\pi^*A^1\Pi$ ); **b** The time-evolution of expectation value of inter-nuclear distance ( $\langle R_{CO} \rangle(\Delta t)$ ) from nuclear revival dynamics on state I; **c** The  $\Delta t$ -dependent resonant Auger electron spectra  $\sigma(\epsilon, \Delta t)$  from a nuclear wavepacket of state I; **d** Auger electron spectra from selected  $\langle R_{CO} \rangle(\Delta t)$  being the left and right turnings; **e** The time-evolution of Auger signal of selected Auger electron energies.

$$\psi_0(q, t) = \sum_i c_i^I e^{i(\varphi_i^I - E_i^I t)} |i^I(q)\rangle, \text{ as}$$

$$\begin{aligned} \sigma(\epsilon, \Delta t)_{\psi_0} &\simeq \sum_i c_i^I c_i^I \sigma_{ii}(\epsilon) \\ &+ \sum_{i>j} \left( 2c_i^I c_j^I \text{Re}(\sigma_{ij}(\epsilon)) \cos(\Delta\varphi_{ij}^I - \Delta E_{ij}^I \Delta t) \right) \\ &+ \sum_{i>j} \left( 2c_i^I c_j^I \text{Im}(\sigma_{ij}(\epsilon)) \sin(\Delta\varphi_{ij}^I - \Delta E_{ij}^I \Delta t) \right), \end{aligned} \quad (1)$$

where  $\Delta E_{ij}^I = E_i^I - E_j^I$  represents the relative energy, and  $\Delta\varphi_{ij}^I = \varphi_i^I - \varphi_j^I$  denotes the relative phase between vibrational states  $|i^I\rangle$  and  $|j^I\rangle$ . In Eq. (1), the first term corresponds to the incoherent contribution of the resonant Auger signal  $\sigma_{ii}(\epsilon)$  (direct photo-emission) from a pure vibrational state  $|i^I\rangle$ , with a weight  $c_i^I c_i^I$  being the square of its population. The second and third term represent the time-dependent coherent contributions arising from the cross interplay  $\sigma_{ij}(\epsilon)$ . The signal  $\sigma_{ij}(\epsilon)$  satisfies  $\sigma_{ij}(\epsilon) =$

$\sum_f \lim_{t \rightarrow \infty} a_f^{F(i)}(\epsilon, t) (a_f^{F(j)}(\epsilon, t))^*$  and is independent of the initial information of the coherent wavepacket but depends on the X-ray parameters. It is worth noting that the same formula in Eq. (1) can be derived from the Kramers-Heisenberg equation<sup>36,57</sup>.

Eq. (1) contains detailed information about the initial coherent wavepacket. To reconstruct the initial wavepacket  $\psi_0$  through TRAS, a possible approach is to fit the measured time-delay Auger signals  $\sigma(\epsilon, \Delta t)_{\psi_0}$  with the calculated signals  $\sigma_{ij}(\epsilon)$  using Eq. (1). In the following, we demonstrate the application of reconstructing the vibrational wavepacket using TRAS in a CO molecule, considering states I, N and F corresponding to the valence-excited state  $5\sigma^{-1}\pi^*A^1\Pi$ , core-excited state  $C1s^{-1}\pi^*1\Pi$ , and final ionic state  $1\pi^{-1}2\Pi$ , respectively.

Directly fitting the TRAS pattern shown in Fig. 1(c) using Eq. (1) presents a caveat. One sees in Eq. (1) that the relative

vibrational energies  $\Delta E_{ij}^I$  are independent of the Auger energy  $\epsilon$ . Therefore, in principle, the number of involved vibrational states and their relative energies  $\Delta E_{ij}^I$  can be determined initially by fitting the time-evolution of spectra for any selected  $\epsilon$  using Eq. (1). This makes a suboptimal use of the available information. To enhance stability across different  $\epsilon$  data, we fit the summed signal over all  $\epsilon$ , denoted as  $S(\Delta t) = \sum_i \sigma(\epsilon_i, \Delta t)$ . A modified formula of

Eq. (1) is utilized for this fitting, expressed as  $S(\Delta t) \simeq s_{00} + \sum_{i>j} r_{ij} \cos(\Delta E_{ij}^I \Delta t) + \sum_{i>j} i_{ij} \sin(\Delta E_{ij}^I \Delta t)$ . Figure 2a illustrates the fitted signals  $S^N(\Delta t)$  for different models with  $N$  vibrational states. Obviously, the two-state model signal  $S^2(\Delta t)$  significantly deviates from the original signal  $S(\Delta t)$ , whereas the three-state ( $S^3(\Delta t)$ ) and four-state ( $S^4(\Delta t)$ ) models exhibit excellent fitting with  $S(\Delta t)$ . The ratio difference  $R_S^N = |1 - S^N/S|$  effectively demonstrates the feasibility of models with varying numbers of vibrational states (Fig. 2b). The ratio difference decreases from approximately  $5 \times 10^{-3}$  for the two-state model to  $10^{-4}$  for the three-state model, and further to  $10^{-6}$  for the four-state model. The fitted vibrational energy values are summarized in Table 1. These values show energy differences of approximately  $10^{-3}$  eV and  $10^{-4}$  eV from the real calculated values, utilizing the potential energy curve of state I ( $5\sigma^{-1}\pi^*A^1\Pi$ ), for the three-state and four-state models, respectively. Fitting with more states ( $N > 4$ ) results in a breakdown of the fitting process, particularly with neighboring states of identical values. Therefore, it can be concluded that the initial wavepacket on state I must involve at least three dominant vibrational states, with four vibrational states being the most plausible scenario.

The algorithms of Levenberg-Marquardt and Universal Global Optimization are employed in fittings implemented in 1stOpt software<sup>58</sup>, which is widely recognized in the field of nonlinear regression and offers a powerful built-in general global

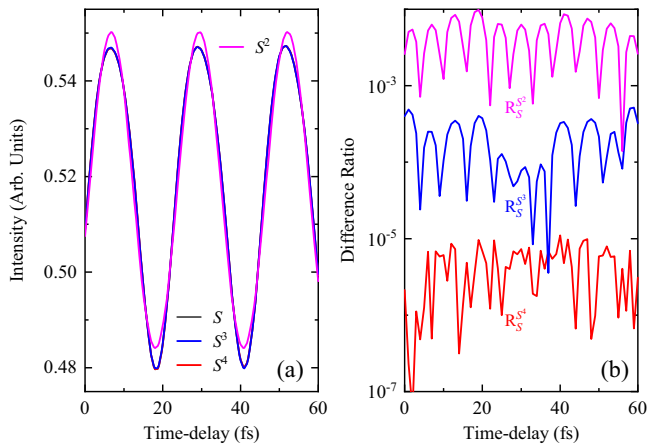


**Fig. 2 Summed signals.** The black lines represent the original summed signal  $S(\Delta t)$ , while the magenta, blue and red lines represent the summed signals  $S^N(\Delta t)$  in two- ( $N = 2$ ), three- ( $N = 3$ ) and four-state ( $N = 4$ ) models, respectively. **a** The summed signal  $S(\Delta t)$  and the fitted one  $S^N(\Delta t)$  with  $N = \{2, 3, 4\}$  indicating the number of vibrational levels used in fitting; **b** The ratio difference  $R_S^N = |1 - S^N/S|$  between the original and fitted signals.

optimization algorithm for parameter collection. The accuracy of fitted parameters is evaluated using a commonly used index in regression analysis, the coefficient of determination ( $R^2$ ), which approaches 1.0 when the fitting results closely resemble the actual calculation results. In our case, the  $R^2$  values for the fitting of two-state model  $S^2(\Delta t)$ , three-state model  $S^3(\Delta t)$ , and four-state model  $S^4(\Delta t)$  shown in Fig. 2a are 0.986329, 0.9999697, and 0.9999999895, respectively. Obviously, as the number of vibrational states increases, the  $R^2$  value tends to approach 1.0, indicating a closer fit between the calculated and actual results.

To determine the relative coefficients and phases of the initial wavepacket  $\psi_0$  using Eq. (1), it is necessary to obtain the signals  $\sigma_{ij}(\epsilon)$  for all the involved vibrational states in advance. The calculation of  $\sigma_{ij}(\epsilon)$  is straightforward and can be obtained by setting the initial state to a specific vibrational state  $|i\rangle$ , where  $i$  ranges from 0 to 3. On the other hand, the cross signal  $\sigma_{ij}(\epsilon)$  can be estimated using two specific coherent wavepackets,  $\psi_1 = (|i\rangle + |j\rangle)/\sqrt{2}$  and  $\psi_2 = (|i\rangle + i|j\rangle)/\sqrt{2}$ . By applying Eq. (1), the real part of  $\sigma_{ij}(\epsilon)$  can be expressed as  $\text{Re}(\sigma_{ij}(\epsilon)) = \sigma_{ij}(\epsilon)\psi_1 - \frac{1}{2}(\sigma_{ii}(\epsilon) + \sigma_{jj}(\epsilon))$ , and the imaginary part as  $\text{Im}(\sigma_{ij}(\epsilon)) = \sigma_{ij}(\epsilon)\psi_2 - \frac{1}{2}(\sigma_{ii}(\epsilon) + \sigma_{jj}(\epsilon))$ . All the relevant data for  $\sigma_{ij}(\epsilon)$  are provided in the Supplementary Data.

Based on Eq. (1), the original TRAS signal  $\sigma(\epsilon, \Delta t)$  is fitted using both the three-state and four-state models with corresponding vibrational energies as listed in Table 1. The ratio difference  $R_\sigma^N = |1 - \sigma^N(\epsilon, \Delta t)/\sigma(\epsilon, \Delta t)|$ , obtained from the fitted spectra  $\sigma^N(\epsilon, \Delta t)$  in the  $N$ -state model, is presented in Fig. 3. The results show that the overall ratio difference is approximately 1% for the three-state model and 0.1% for the four-state model. Table 2 provides the fitted relative coefficients and phases. We find that both models yield values of the coefficients for the first three states that are in close agreement. Surprisingly, the four-state model also predicts a minor contribution (0.01% population) from the fourth state, which differs from the original values (obtained by projecting the initial wavepacket onto each vibrational state of state I ( $5\sigma^{-1}\pi^*A^1\Pi$ )) in the fourth decimal place. Regarding the relative phases, the three-state and four-state models differ from the original values in the second and third decimal places, respectively. In the absence of any information regarding the initial wavepacket for comparison,

**Table 1 Rebuilding the vibrational energy from summed signals.**

	$\Delta E_{10}^I$	$\Delta E_{21}^I$	$\Delta E_{32}^I$
Two-state	0.182317		
Three-state	0.182283	0.180372	
Four-state	0.183542	0.179707	0.166836
Original	0.183378	0.179847	0.166515

The fitted relative vibrational energy (eV) of state I ( $5\sigma^{-1}\pi^*A^1\Pi$ ) in two-, three- and four-state models from Fig. 2, the original ones are achieved by diagonalizing the potential of state I.

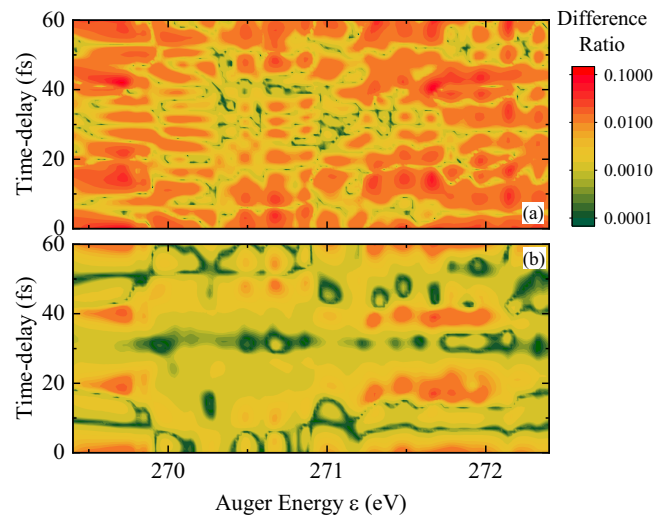


**Fig. 3 Ratio difference.** The ratio difference  $R_\sigma^N = |1 - \sigma^N(\epsilon, \Delta t)/\sigma(\epsilon, \Delta t)|$  between the original spectra  $\sigma(\epsilon, \Delta t)$  and the fitted ones in **(a)** three-state  $\sigma^3(\epsilon, \Delta t)$  and **(b)** four-state  $\sigma^4(\epsilon, \Delta t)$  models.

it can be concluded that both the three-state and four-state models perform well. The four-state model achieves an accuracy of population prediction within 0.01%. Furthermore, the  $R^2$  values for the three-state and four-state models are 0.9996943 and 0.9999909561, respectively. These results confirm the feasibility and accuracy of using TRAS for reconstructing the nuclear wavepacket in both forward and backward directions.

**Reconstruction from blurred TRAS.** To account for the unexpected instabilities in measurements such as energy resolution, temporal jitters or other external disturbances, we blur the TRAS spectra  $\sigma(\epsilon, \Delta t)$  (shown in Fig. 1(c)) by multiplying a random mask function  $R_k(\epsilon, \Delta t)$  (its value is randomly generated in  $[1.0 - k, 1.0 + k]$ ) by both seeds  $\epsilon$  and  $\Delta t$ , and produce the blurred signal  $\sigma_k(\epsilon, \Delta t) = \sigma(\epsilon, \Delta t) \times R_k(\epsilon, \Delta t)$  as well as the summed signal as  $S_k(\Delta t) = \sum_i \sigma_k(\epsilon_i, \Delta t)$ . The instability  $k = 1\%$  and  $5\%$  are evaluated in the following, corresponding to cases with minor and intermediate instabilities. Please refer to Supplementary Fig. s1 in Supplementary Note 1 for the blurred signals  $\sigma_k(\epsilon, \Delta t)$ .

Figure 4a and c show the summed signals  $S_k(\Delta t)$  for the blurred spectra with  $k = 1\%$  and  $5\%$  and the fitted ones in three-state ( $S_k^3(\Delta t)$ ) and four-state ( $S_k^4(\Delta t)$ ) models. It shows the signal  $S_{5\%}(\Delta t)$  is no longer smooth. Figure 4b and d suggests that the ratio difference ( $R_{S_k}^N = |1 - S_k^N/S_k|$ ) differs not too much for the models, but positively correlates with the instability in measurements. These have been reflected in the  $R^2$  values, which are 0.99978875 and 0.99981915 for the three-state and four-state models, respectively, with  $k = 1\%$ , and more closer to 1.0 than



**Table 2 Rebuilding the coefficients and relative phases from Time-resolved resonant Auger-electron spectroscopy.**

	$c_0^1$	$c_1^1$	$c_2^1$	$c_3^1$	$\Delta\varphi_{10}^1$	$\Delta\varphi_{20}^1$	$\Delta\varphi_{30}^1$
Three-state	0.8436	0.5264	0.1062		2.6767	-0.7190	
Four-state	0.8431	0.5267	0.1077	0.0108	2.7371	-0.6967	2.5961
Original	0.8431	0.5269	0.1075	0.0107	2.7276	-0.7024	2.5790

The coefficients and relative phases of the initial wavepacket by fitting  $\sigma(\epsilon, \Delta t)$  using Eq. (1) in three- and four-state models from Fig. 3, the values of original are achieved by projecting the initial wavepacket to each vibrational states of state 1 ( $5\sigma^{-1}\pi^2 A^{\dagger}T$ ).

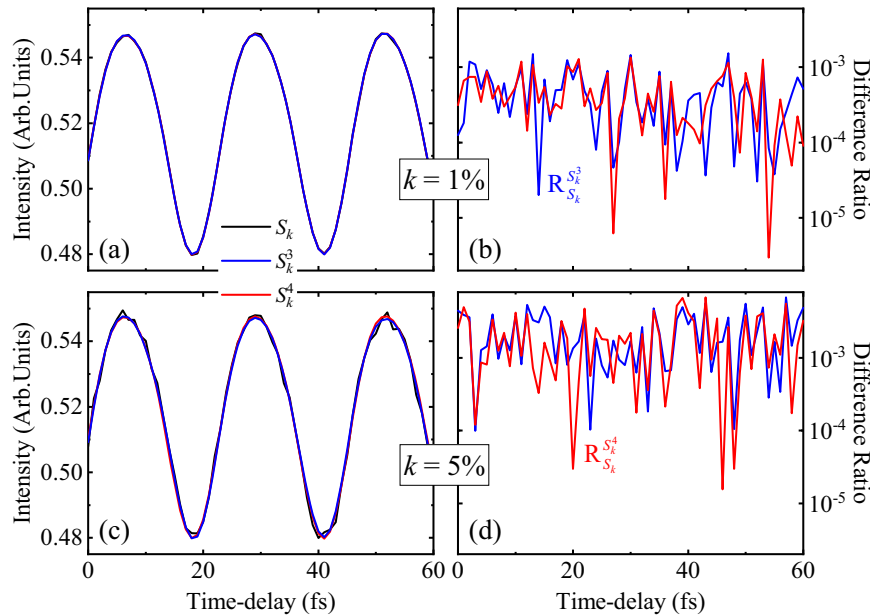


**Fig. 4 Summed signals for blurred spectra.** The black lines represent the original summed signal  $S_k(\Delta t)$  ( $k=1\%$  or  $5\%$ ), while the blue and red lines represent the summed signals  $S_k^N(\Delta t)$  in three- ( $N=3$ ) and four-state ( $N=4$ ) models, respectively. **a** The summed signal  $S_k(\Delta t)$  and the fitting one  $S_k^3(\Delta t)$  ( $N=\{3, 4\}$ ) for the blurred spectra with instability  $k=1\%$ ; **b** The ratio difference  $R_{S_k^3}^{S_k} = |1 - S_k^3/S_k|$  in the fitting for the blurred spectra with instability  $k=1\%$ . **c** and **d** are the same as **a** and **b**, respectively, but  $k=5\%$ .

**Table 3 Reconstruction the vibrational energy from blurred spectra.**

$k$		$\Delta E_{10}^1$	$\Delta E_{21}^1$	$\Delta E_{32}^1$
1%	Three-state	0.182184	0.180510	
5%	Three-state	0.182914	0.180734	
1%	Four-state	0.183001	0.179501	0.166157
5%	Four-state	0.183703	0.181000	0.165001
	original	0.183378	0.179847	0.166515

Same as in Table 1 but in three- and four-state models from Fig. 4 of the summed signals for blurred spectra with instabilities  $k=1\%$  and  $5\%$ .

0.995671 and 0.996274 for the three-state and four-state models, respectively, with  $k=5\%$ . Table 3 presents the collected vibrational energies from Fig. 4, after considering the instability in measurements. The energy difference compared to the original calculations can still be maintained within the range of  $10^{-3}$  to  $10^{-4}$  eV.

Subsequently, the blurred TRAS signal  $\sigma_k(\epsilon, \Delta t)$  are fitted using both three- and four-state models, and Fig. 5 illustrates the ratio difference ( $R_{\sigma_k^N}^{\sigma_k} = |1 - \sigma_k^N(\epsilon, \Delta t)/\sigma_k(\epsilon, \Delta t)|$ ), which remains within the range of 1% to 0.1% for  $k=1\%$ . However, for  $k=5\%$  the ratio difference significantly exceeds 1% and reaches about 10%. These are consistent with the  $R^2$  values of 0.9999038073 and 0.9981426 in the four-state model for  $k=1\%$

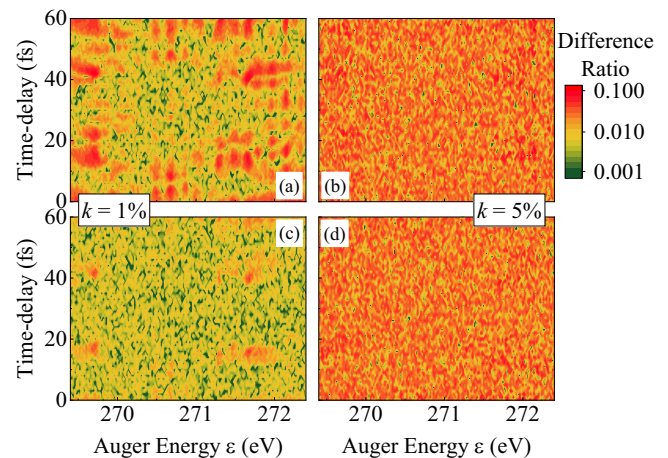


**Fig. 5 Ratio difference for blurred spectra.** The ratio difference  $R_{\sigma_k^N}^{\sigma_k} = |1 - \sigma_k^N(\epsilon, \Delta t)/\sigma_k(\epsilon, \Delta t)|$  between the blurred spectra  $\sigma_k(\epsilon, \Delta t)$  and fitted ones in three-state ( $\sigma_k^3(\epsilon, \Delta t)$ , **a** and **b** panels) and four-state ( $\sigma_k^4(\epsilon, \Delta t)$ , **c** and **d** panels) models with instability  $k=1\%$  (**a** and **c** panels) and  $k=5\%$  (**b** and **d** panels).

and 5%, respectively. Furthermore, the relative coefficients and phases, as shown in Table 4, demonstrate that the three- and four-state models can still be fitted with both  $k=1\%$  and 5%. The simulations suggest that the relative phases are sensitive to both

**Table 4 Reconstruction the coefficients and relative phases from blurred spectra.**

$k$		$c_0^I$	$c_1^I$	$c_2^I$	$c_3^I$	$\Delta\varphi_{10}^I$	$\Delta\varphi_{20}^I$	$\Delta\varphi_{30}^I$
1%	Three-state	0.8443	0.5269	0.1063		2.6740	-0.7112	
5%	Three-state	0.8440	0.5281	0.1081		2.7098	-0.6697	
1%	Four-state	0.8442	0.5270	0.1071	0.0105	2.7122	-0.7289	2.5450
5%	Four-state	0.8437	0.5282	0.1091	0.0112	2.7465	-0.6311	2.6542
	Original	0.8431	0.5269	0.1075	0.0107	2.7276	-0.7024	2.5790

Same as in Table 2 but in three- and four-state models from Fig. 5 of the blurred spectra with instabilities  $k=1\%$  and  $5\%$ .

the fitting model and the noise: the better of fitting model and the smaller of noise, the closer the retrieved phase to the reference data. The retrieved results from the blurred spectra are encouraging, further demonstrating the feasibility of using TRAS for reconstructing the vibronic dynamics.

Considering the experimental energy resolution may be worse, simulations with bigger instability as  $k=10\%$  and  $k=20\%$  are also implemented and given in Supplementary Note 1. As it shows clearly, worse energy resolution reduces the accuracy of extracted wavepacket data.

## Conclusions

Thanks to the energy resolution of RAS, determined by the Auger lifetime, time-resolved RAS improves on the comparatively low energy resolution of time-resolved photo-electron spectroscopy by ultrashort X-ray pulses. We show that the signal of time-resolved resonant Auger-electron spectroscopy using attosecond X-ray pulses still contains enough information to rebuild coherent wavepacket dynamics. The derived simple relationship offers a promising approach to retrieving and reconstructing the complete information of the initial coherent wavepacket. By applying this framework to a CO molecule, we demonstrate the feasibility and accuracy of reconstructing the full information of the vibrational wavepacket created by the pump pulse. This includes the relative energies, populations, and phases of the vibrational states, even when the signals are blurred by significant random noise.

We should note that the present method also works when the Auger decay width is larger than the energy separation between the vibrational levels. In Supplementary Note 2 (Supplementary Fig. s2), we artificially increase the Auger decay width of CO from 0.08 eV to 0.4 eV. The corresponding TRAS spectra lose the ability to resolve vibrational structures but they are still sensitive to the time-delay of the initial wavepacket. The information on the initial wavepacket can still be reconstructed as shown in Supplementary Table s1 and Table s2 in Supplementary Note 2. This result can be understood from the fact that Eq. (1) does not explicitly depend on the Auger decay width. This methodology can be extended without further modification to investigate attosecond electronic dynamics using attosecond X-ray pulses. Given the widespread interest in tracking nuclear and electronic dynamics in ultrafast physics and photochemistry, this work opens up new possibilities for the application of femtosecond and attosecond X-ray probe pulses.

## Methods

Let us consider a diatomic molecule initially in electronic state I and excited by a X-ray pulse to the Auger electronic state N. The ensuing Auger decay emits an electron with energy  $\varepsilon$  to ionic electronic state F.  $|\nu^\gamma(q)\rangle$  and  $E_\nu^\gamma$  are vibrational wavefunction and energy of each electronic state  $\gamma = \{I, N, F\}$ . Following the theoretical frame for few-level system<sup>40,54</sup>, the total time-dependent wavefunction of the system reads  $\psi(q, t) = \sum_i a_i^I$

$(t)|i^I(q)\rangle + \sum_n a_n^N(t)|n^N(q)\rangle + \sum_f \int d\varepsilon a_f^F(\varepsilon, t)|\varepsilon\rangle|f^F(q)\rangle$ , where  $|\varepsilon\rangle$

indicates the free wavefunction of Auger electron,  $a_f^F(t)$  is the amplitude of vibrational level  $|\nu^f(q)\rangle$ . After inserting  $\psi(q, t)$  into the time-dependent Schrödinger equation for the total interaction Hamiltonian and employing the local approximation<sup>59,60</sup>, we reach the evolution equation for the amplitudes as  $\dot{\tilde{\psi}}(\varepsilon, t) = \bar{H}(\varepsilon, t)\tilde{\psi}(\varepsilon, t)$  with  $\tilde{\psi}(\varepsilon, t) = [\{a_i^I(t)\}, \{a_n^N(t)\}, \{a_f^F(\varepsilon, t)\}]^T$  ( $\{\}$  is the simplified notation for all possible vibrational states), and the dressed Hamiltonian

$$\bar{H}(\varepsilon, t) = \begin{pmatrix} \{E_i^I\} & \{V_{in}^{NI}\} & 0 \\ \{V_{ni}^{NI}(t)\} & \{E_n^N - \frac{i\Gamma}{2}\} & 0 \\ 0 & \{V_{fn}^{FN}\} & \{E_f^F + \varepsilon\} \end{pmatrix}, \quad (2)$$

where  $V_{fn}^{FN} = \sqrt{\frac{\Gamma}{2\pi}} \langle f^F(q)|n^N(q)\rangle$  is the efficient Coulomb interaction matrix weighted by the Franck-Condon factor  $\langle f^F(q)|n^N(q)\rangle$  from state  $|n^N(q)\rangle$  to state  $|f^F(q)\rangle$ ,  $V_{ni}^{NI}(t) = g_0 g(t, \Delta t) \cos(\omega t) d_{NI} \langle f^N(q)|n^I(q)\rangle$  is the laser dipole interaction with  $d_{NI}$  being the electronic transition dipole moment.  $g_0, g(t, \Delta t) = e^{-4 \ln 2 (t - \Delta t)^2 / \tau^2}$ ,  $\omega, \tau$  and  $\Delta t$  are the peak intensity, envelope, frequency, duration, and pulse centre, respectively. If the molecule is in state  $|i^I(q)\rangle$  at time zero, in the weak field limit  $a_f^F(\varepsilon, t) = a_i^I(\Delta t) a_f^{F(i)}(\varepsilon, t)$  can be well represented by second-order time-dependent perturbation theory as

$$a_f^{F(i)}(\varepsilon, t) \simeq - \sum_n \int_{-\infty, -\infty}^{t, t'} dt' dt'' e^{i\omega_{fn}^{FN} t'} V_{fn}^{FN} e^{i\omega_{ni}^{NI} t''} V_{ni}^{NI}(t''), \quad (3)$$

where  $\omega_{fn}^{FN} = E_f^F - E_n^N + \varepsilon + \frac{i\Gamma}{2}$ ,  $\omega_{ni}^{NI} = E_n^N - E_i^I - \frac{i\Gamma}{2}$ , then the total Auger electron spectrum can be calculated as the sum over all final states for the norm square of  $a_f^F$  in the long time limit as  $\sigma(\varepsilon) = \sum_f \lim_{t \rightarrow \infty} |a_f^F(\varepsilon, t)|^2 = |a_i^I(\Delta t)|^2 \sum_f \lim_{t \rightarrow \infty} |a_f^{F(i)}(\varepsilon, t)|^2$ .

We should note that the above method can, in principle, be modified and applied to polyatomic molecules. The case of a separable nuclear Schrodinger equation in normal modes<sup>61-63</sup> can be readily considered and we note that normal modes are good coordinates for photochemical processes at short times<sup>64-67</sup>. If the relevant normal-mode coordinates are  $\{q_Q\} (Q=1, \dots, Q_T)$  and are well localized as harmonic oscillators, the initial coherent wavefunction could be written as

$$\begin{aligned} \psi_0(\{q_Q\}, \Delta t) &= \prod_{Q=1} \sum_i a_{i_Q}^I(\Delta t) |i_Q^I(q_Q)\rangle, \\ a_{i_Q}^I(\Delta t) &= c_{i_Q}^I e^{i(\varphi_{i_Q}^I - E_{i_Q}^I \Delta t)} \end{aligned} \quad (4)$$

where  $c_{i_Q}^I, \varphi_{i_Q}^I$  and  $E_{i_Q}^I$  represent the initial coefficient, initial phase and energy of vibrational state  $|i_Q^I(q_Q)\rangle$  of each normal mode  $q_Q$ , respectively. As presented in Supplementary Note 3, the  $\Delta t$ -dependent Auger signal could be written as the incoherent

contributions from each normal mode as

$$\sigma(\varepsilon, \Delta t) = \sum_{Q=1} \sigma_Q(\varepsilon, \Delta t), \quad (5)$$

with

$$\begin{aligned} \sigma_Q(\varepsilon, \Delta t) \simeq & \sum_i c_{iQ}^I c_{iQ}^I \sigma_{i_{iQ}}(\varepsilon) \\ & + \sum_{i>j} \left( 2c_{iQ}^I c_{jQ}^I \operatorname{Re}(\sigma_{i_{iQ}}(\varepsilon)) \cos(\Delta\varphi_{i_{iQ}}^I - \Delta E_{i_{iQ}}^I \Delta t) \right) \\ & + \sum_{i>j} \left( 2c_{iQ}^I c_{jQ}^I \operatorname{Im}(\sigma_{i_{iQ}}(\varepsilon)) \sin(\Delta\varphi_{i_{iQ}}^I - \Delta E_{i_{iQ}}^I \Delta t) \right). \end{aligned} \quad (6)$$

It might as well be possible to work directly at the level of the correlated vibronic eigenstates for multidimensional problems, thus obviating any underlying separability. These cases can turn up to be quite challenging if the density of vibronic states is high. Future investigations shall consider how much of this information can still be retrieved by carefully fitting the TRAS signal to sensible models of the vibronic wavepacket.

### Data availability

Data that support the plots within this paper and other findings of this study are available from the accompanying Supplementary Notes. The original spectra and all incoherent contributions from a pure vibrational state and coherent contributions from the cross interplay are provided as Supplementary Data 1 and 2. Any additional detail can be obtained from the corresponding authors upon reasonable request.

### Code availability

The codes associated with this manuscript are available from the corresponding author on reasonable request.

Received: 17 July 2023; Accepted: 18 December 2023;  
Published online: 02 January 2024

### References

- Blanchet, V., Zgierski, M. Z., Seideman, T. & Stolow, A. Discerning vibronic molecular dynamics using time-resolved photoelectron spectroscopy. *Nature* **401**, 52–54 (1999).
- Wörner, H. J., Bertrand, J. B., Kartashov, D. V., Corkum, P. B. & Villeneuve, D. M. Following a chemical reaction using high-harmonic interferometry. *Nature* **466**, 604–607 (2010).
- Kobayashi, Y., Chang, K. F., Zeng, T., Neumark, D. M. & Leone, S. R. Direct mapping of curve-crossing dynamics in IBR by attosecond transient absorption spectroscopy. *Science* **365**, 79–83 (2019).
- Stapelheldt, H. & Seideman, T. Colloquium: Aligning molecules with strong laser pulses. *Rev. Mod. Phys.* **75**, 543–557 (2003).
- Stolow, A., Bragg, A. E. & Neumark, D. M. Femtosecond time-resolved photoelectron spectroscopy. *Chem. Rev.* **104**, 1719–1758 (2004).
- Krausz, F. & Ivanov, M. Attosecond physics. *Rev. Mod. Phys.* **81**, 163–234 (2009).
- Kraus, P. M., Zürich, M., Cushing, S. K., Neumark, D. M. & Leone, S. R. The ultrafast x-ray spectroscopic revolution in chemical dynamics. *Nat. Rev. Chem.* **2**, 82–94 (2018).
- Pellegrini, C., Marinelli, A. & Reiche, S. The physics of x-ray free-electron lasers. *Rev. Mod. Phys.* **88**, 015006 (2016).
- Seddon, E. A. et al. Short-wavelength free-electron laser sources and science: a review\*. *Rep. Prog. Phys.* **80**, 115901 (2017).
- Lu, W. et al. Development of a hard x-ray split-and-delay line and performance simulations for two-color pump-probe experiments at the European XFEL. *Rev. Sci. Instrum.* **89**, 063121 (2018).
- Rossbach, J., Schneider, J. R. & Wurth, W. 10 years of pioneering x-ray science at the free-electron laser flash at desy. *Phys. Rep.* **808**, 1–74 (2019).
- Malychenkov, A. et al. Single- and two-color attosecond hard x-ray free-electron laser pulses with nonlinear compression. *Phys. Rev. Res.* **2**, 042018 (2020).
- Duris, J. et al. Tunable isolated attosecond x-ray pulses with gigawatt peak power from a free-electron laser. *Nat. Photonics* **14**, 30–36 (2020).
- Callegari, C. et al. Atomic, molecular and optical physics applications of longitudinally coherent and narrow bandwidth free-electron lasers. *Phys. Rep.* **904**, 1–59 (2021).
- Saito, N. et al. Real-time observation of electronic, vibrational, and rotational dynamics in nitric oxide with attosecond soft x-ray pulses at 400eV. *Optica* **6**, 1542–1546 (2019).
- Lin, S.-C. et al. Operando time-resolved x-ray absorption spectroscopy reveals the chemical nature enabling highly selective CO<sub>2</sub> reduction. *Nat. Commun.* **11**, 3525 (2020).
- Jadoun, D. & Kowalewski, M. Time-resolved photoelectron spectroscopy of conical intersections with attosecond pulse trains. *J. Phys. Chem. Lett.* **12**, 8103–8103 (2021).
- Pathak, S. et al. Tracking the ultraviolet-induced photochemistry of thiophenone during and after ultrafast ring opening. *Nat. Chem.* **12**, 795–800 (2020).
- LaForge, A. C. et al. Ultrafast resonant interatomic coulombic decay induced by quantum fluid dynamics. *Phys. Rev. X* **11**, 021011 (2021).
- Fushitani, M. et al. Time-resolved photoelectron imaging of complex resonances in molecular nitrogen. *J. Chem. Phys.* **154**, 144305 (2021).
- Waters, M. D. J. et al. Transient symmetry controls photo dynamics near conical intersections. *J. Phys. Chem. Lett.* **12**, 9220–9225 (2021).
- Kastirke, G. et al. Photoelectron diffraction imaging of a molecular breakup using an x-ray free-electron laser. *Phys. Rev. X* **10**, 021052 (2020).
- Ota, F. et al. Imaging intramolecular hydrogen migration with time- and momentum-resolved photoelectron diffraction. *Phys. Chem. Chem. Phys.* **23**, 20174–20182 (2021).
- Ota, F., Yamazaki, K., Sébilleau, D., Ueda, K. & Hatada, K. Theory of polarization-averaged core-level molecular-frame photoelectron angular distributions: Iii. new formula for p- and s-wave interference analogous to Young's double-slit experiment for core-level photoemission from hetero-diatom molecules. *J. Phys. B: At. Mol. Opt. Phys.* **54**, 244002 (2022).
- Keefer, D., Schnappinger, T., de Vivie-Riedle, R. & Mukamel, S. Visualizing conical intersection passages via vibronic coherence maps generated by stimulated ultrafast x-ray Raman signals. *Proc. Natl. Acad. Sci.* **117**, 24069–24075 (2020).
- Cho, D., Rouxel, J. R. & Mukamel, S. Stimulated x-ray resonant Raman spectroscopy of conical intersections in thiophenol. *J. Phys. Chem. Lett.* **11**, 4292–4297 (2020).
- Haldrup, K. et al. Ultrafast x-ray scattering measurements of coherent structural dynamics on the ground-state potential energy surface of a diplatinum molecule. *Phys. Rev. Lett.* **122**, 063001 (2019).
- Stankus, B. et al. Ultrafast x-ray scattering reveals vibrational coherence following Rydberg excitation. *Nat. Chem.* **11**, 716–721 (2019).
- Kunnus, K. et al. Vibrational wavepacket dynamics in fe carbene photosensitizer determined with femtosecond x-ray emission and scattering. *Nat. Commun.* **11**, 634 (2020).
- Yong, H. et al. Ultrafast X-ray scattering offers a structural view of excited-state charge transfer. *Proceedings of the National Academy of Sciences* **118**, e2021714118 (2021).
- Keefer, D. et al. Imaging conical intersection dynamics during azobenzene photoisomerization by ultrafast x-ray diffraction. *Proc. Natl. Acad. Sci.* **118**, e2022037118 (2021).
- Yong, H., Keefer, D. & Mukamel, S. Imaging purely nuclear quantum dynamics in molecules by combined x-ray and electron diffraction. *J. Am. Chem. Soc.* **144**, 7796–7804 (2022).
- Panman, M. R. et al. Observing the structural evolution in the photodissociation of diiodomethane with femtosecond solution x-ray scattering. *Phys. Rev. Lett.* **125**, 226001 (2020).
- Kim, K. H. et al. Solvent-dependent molecular structure of ionic species directly measured by ultrafast x-ray solution scattering. *Phys. Rev. Lett.* **110**, 165505 (2013).
- Lee, Y. et al. Ultrafast coherent motion and helix rearrangement of homodimeric hemoglobin visualized with femtosecond x-ray solution scattering. *Nat. Commun.* **12**, 3677 (2021).
- Gel'mukhanov, F., Odelius, M., Polyutov, S. P., Föhlisch, A. & Kimberg, V. Dynamics of resonant x-ray and auger scattering. *Rev. Mod. Phys.* **93**, 035001 (2021).
- Feifel, R. et al. Profile of resonant photoelectron spectra versus the spectral function width and photon frequency detuning. *Phys. Rev. A* **70**, 032708 (2004).
- Zhu, Y. P., Zhao, X., Liu, X.-J., Kimberg, V. & Zhang, S. B. Coincidence spectroscopy of molecular normal auger decay by ultrashort x-ray pulses. *Phys. Rev. A* **106**, 023105 (2022).
- Demekhin, P. V., Chiang, Y.-C. & Cederbaum, L. S. Resonant auger decay of the core-excited c\*o molecule in intense x-ray laser fields. *Phys. Rev. A* **84**, 033417 (2011).
- Zhang, S. B. & Rohringer, N. Quantum-beat auger spectroscopy. *Phys. Rev. A* **92**, 043420 (2015).

41. Zhang, S. B., Kimberg, V. & Rohringer, N. Nonlinear resonant auger spectroscopy in co using an x-ray pump-control scheme. *Phys. Rev. A* **94**, 063413 (2016).
42. Freibert, A., Mendive-Tapia, D., Huse, N. & Vendrell, O. Femtosecond X-ray absorption spectroscopy of pyrazine at the nitrogen K-edge: On the validity of the Lorentzian limit. *J. Phys. B: At., Mol. Opt. Phys.* **54**, 244003 (2021).
43. Wang, C. et al. Time-resolved resonant auger scattering clocks distortion of a molecule. *J. Phys. Chem. Lett.* **14**, 5475–5480 (2023).
44. Nan, Q.-W. et al. Resonant auger scattering by attosecond x-ray pulses. *Chin. Phys. Lett.* **40**, 093201 (2023).
45. Goulielmakis, E. et al. Real-time observation of valence electron motion. *Nature* **466**, 739–743 (2010).
46. Ott, C. et al. Reconstruction and control of a time-dependent two-electron wave packet. *Nature* **516**, 374–378 (2014).
47. Peng, P. et al. Coherent control of ultrafast extreme ultraviolet transient absorption. *Nat. Photonics* **16**, 45–51 (2022).
48. Wei, Z. et al. Elucidating the origins of multimode vibrational coherences of polyatomic molecules induced by intense laser fields. *Nat. Commun.* **8**, 735 (2017).
49. Timmers, H. et al. Disentangling conical intersection and coherent molecular dynamics in methyl bromide with attosecond transient absorption spectroscopy. *Nat. Commun.* **10**, 3133 (2019).
50. Nabekawa, Y. et al. Settling time of a vibrational wavepacket in ionization. *Nat. Commun.* **6**, 8197 (2015).
51. Bello, R. Y. et al. Reconstruction of the time-dependent electronic wave packet arising from molecular autoionization. *Sci. Adv.* **4**, eaat3962 (2018).
52. Kraus, P. M. et al. Measurement and laser control of attosecond charge migration in ionized iodoacetylene. *Science* **350**, 790–795 (2015).
53. Skytt, P. et al. Role of screening and angular distributions in resonant x-ray emission of co. *Phys. Rev. A* **55**, 134–145 (1997).
54. Pahl, E., Meyer, H.-D. & Cederbaum, L. Competition between excitation and electronic decay of short-lived molecular states. *Z. Phys. D: At., Mol. Clusters* **38**, 215–232 (1996).
55. Demekhin, P. V. & Cederbaum, L. S. Resonant auger decay of core-excited co molecules in intense x-ray laser pulses: the o ( $1s \rightarrow \pi^*$ ) excitation. *J. Phys. B: At., Mol. Opt. Phys.* **46**, 164008 (2013).
56. Worth, G. A., Beck, M. H., Jäckle, A., Vendrell, O. & Meyer, H.-D. The MCTDH Package. Version 8.2, (2000). H.-D. Meyer, Version 8.3 (2002), Version 8.4 (2007). O. Vendrell and H.-D. Meyer Version 8.5 (2013). Version 8.5 contains the ML-MCTDH algorithm. Current versions: 8.4.18 and 8.5.11 (2019). Used version: exchange with “Used version” See <http://mctdh.uni-hd.de/>.
57. Correia, N. et al. Theory of band shape formation in auger and autoionization spectra of molecules. numerical applications and new high-resolution spectra for co. *J. Chem. Phys.* **83**, 2035–2052 (1985).
58. 7D-Soft Hi-Tech Inc. 1stOpt Software Platform. Current versions: Version 10.0 (2022). Used version: See <http://www.7d-soft.com/>.
59. Cederbaum, L. S. & Domcke, W. Local against non-local complex potential in resonant electron-molecule scattering. *J. Phys. B: At. Mol. Opt. Phys.* **14**, 4665 (1981).
60. Demekhin, P. V. & Cederbaum, L. S. Strong interference effects in the resonant auger decay of atoms induced by intense x-ray fields. *Phys. Rev. A* **83**, 023422 (2011).
61. Hänggi, P., Talkner, P. & Borkovec, M. Reaction-rate theory: fifty years after Kramers. *Rev. Mod. Phys.* **62**, 251–341 (1990).
62. Atkins, P. & Friedman, R. *Molecular Quantum Mechanics (4th)* (Oxford University Press, New York, 2005).
63. Prigogine, I. & Rice, S. A. *Advances in chemical physics* (John Wiley & Sons, Inc., New York, 2009).
64. Raab, A., Worth, G. A., Meyer, H.-D. & Cederbaum, L. Molecular dynamics of pyrazine after excitation to the s2 electronic state using a realistic 24-mode model Hamiltonian. *J. Chem. Phys.* **110**, 936 (1999).
65. Vallet, V., Lan, Z., Mahapatra, S., Sobolewski, A. L. & Domcke, W. Photochemistry of pyrrole: Time-dependent quantum wave-packet description of the dynamics at the  $\pi\sigma^*$ -s conical intersections. *J. Chem. Phys.* **123**, 144307 (2005).
66. Beck, M., Jäckle, A., Worth, G. & Meyer, H.-D. The multiconfiguration time-dependent hartree (MCTDH) method: a highly efficient algorithm for propagating wavepackets. *Phys. Rep.* **324**, 1–105 (2000).
67. Hua, W., Mukamel, S. & Luo, Y. Transient x-ray absorption spectral fingerprints of the s1 dark state in uracil. *J. Phys. Chem. Lett.* **10**, 7172 (2019).

## Acknowledgements

Grants from NSFC (Nos. 12374238, 11934004, 11974230) are acknowledged. VK acknowledges financial support from the Swedish Research Council (No. 2019-03470).

## Author contributions

S.B.Z. conceived and supervised this project; C.W., X.Y.Y., Q.W.N. and S.B.Z. performed all the simulations; S.B.Z., C.W., M.M.G., X.Z., V.K., O.V., K.U., Y.J.C. and X.J.L. analyzed data and discussed the results; S.B.Z., C.W., M.M.G., X.Z., V.K., O.V. and K.U. wrote the paper.

## Competing interests

The authors declare no competing interests.

## Additional information

**Supplementary information** The online version contains supplementary material available at <https://doi.org/10.1038/s42005-023-01507-3>.

**Correspondence** and requests for materials should be addressed to Song Bin Zhang.

**Peer review information** : *Communications Physics* thanks the anonymous reviewers for their contribution to the peer review of this work.

**Reprints and permission information** is available at <http://www.nature.com/reprints>

**Publisher's note** Springer Nature remains neutral with regard to jurisdictional claims in published maps and institutional affiliations.



**Open Access** This article is licensed under a Creative Commons Attribution 4.0 International License, which permits use, sharing, adaptation, distribution and reproduction in any medium or format, as long as you give appropriate credit to the original author(s) and the source, provide a link to the Creative Commons license, and indicate if changes were made. The images or other third party material in this article are included in the article's Creative Commons license, unless indicated otherwise in a credit line to the material. If material is not included in the article's Creative Commons license and your intended use is not permitted by statutory regulation or exceeds the permitted use, you will need to obtain permission directly from the copyright holder. To view a copy of this license, visit <http://creativecommons.org/licenses/by/4.0/>.

© The Author(s) 2024